Tuning the Selectivity of Nitrate Reduction via Fine Composition Control of RuPdNP Catalysts

Jacob P. Troutman, Jagannath Sai Pavan Mantha, Hao Li, Graeme Henkelman,* Simon M. Humphrey,* and Charles J. Werth*

Herein, aqueous nitrate (NO_3^-) reduction is used to explore composition-selectivity relationships of randomly alloyed ruthenium-palladium nanoparticle catalysts to provide insights into the factors affecting selectivity during this and other industrially relevant catalytic reactions. NO_3^- reduction proceeds through nitrite (NO_2^-) and then nitric oxide (NO), before diverging to form either dinitrogen (N_2) or ammonium (NH_4^+) as final products, with N_2 preferred in potable water treatment but NH_4^+ preferred for nitrogen recovery. It is shown that the NO_3^- and NO starting feedstocks favor NH_4^+ formation using Ru-rich catalysts, while Pd-rich catalysts favor N_2 formation. Conversely, a NO_2^- starting feedstock favors NH_4^+ at ≈50 atomic-% Ru and selectivity decreases with higher Ru content. Mechanistic differences have been probed using density functional theory (DFT). Results show that, for NO_3^- and NO feedstocks, the thermodynamics of the competing pathways for N–H and N–N formation lead to preferential NH_4^+ or N_2 production, respectively, while Ru-rich surfaces are susceptible to poisoning by NO_2^- feedstock, which displaces H atoms. This leads to a decrease in overall reduction activity and an increase in selectivity toward N_2 production. Together, these results demonstrate the importance of tailoring both the reaction pathway thermodynamics and initial reactant binding energies to control overall reaction selectivity.

1. Introduction

Traditional, colloidal heterogeneous catalysts are crucial in increasing the reaction rates and efficiencies for a great number of industrially relevant reactions. The ever increasing demands upon global energy, natural resources, and chemical products—combined with the need to limit society's impact on the environment—means that controlling catalyst selectivity remains at the forefront of nanoscience and catalysis research.[1–4] Catalyst selectivity can be tuned by significantly lowering the barrier of a desired reaction pathway with respect to other potential pathways.[5] However, exerting control over catalyst selectivity presents a greater challenge than increasing the relative catalytic activity. This is because it is more challenging to specify which reaction pathway(s) are followed in instances where multiple pathways with disparate energy barriers co-exist. It is comparatively much easier to exert control over a single rate-limiting energy barrier in order to achieve activity improvements. The ability to exert sufficient control over competing reaction pathways is often hindered by the scaling relationships between adsorbate species involved in chemical reactions (i.e., the relationships between binding energies of the different adsorbate species), which limit the tunability of catalyst selectivity.[6–8] There are a number of approaches to break these scaling relations and improve catalyst selectivity, including tuning the catalyst surface structure,[9–12] or by changing the reaction conditions (pressure, temperature, solvent, etc.).[13–16] The reduction of nitrate (NO_3^-) to ammonium (NH_4^+) in drinking water treatment is a prime example of the importance of catalyst selectivity for nutrient recovery.

Nitrate is one of the most pervasive contaminants in global surface and groundwaters;[17–20] it is found naturally in the environment at concentrations ≤ 1 mg-N L^{-1}.[21] However, NO_3^- levels are often much higher, in large part due to over-application of nitrogen-rich fertilizers coupled with poor nitrogen uptake by crops.[22–24] A 12-year study by the US Geological Survey (USGS) National Water Quality Assessment Program (NAWQA) found that 50% of tested drinking water wells had NO_3^- levels above 1 mg-N L^{-1}, and 8% of wells had NO_3^- concentrations above the

J. P. Troutman[+], C. J. Werth
Department of Civil
Architectural, and Environmental Engineering
The University of Texas at Austin
301 E. Dean Keeton Street Stop C1700, Austin, TX 78712, USA
E-mail: werth@utexas.edu
J. P. Troutman[+], J. S. P. Mantha, G. Henkelman, S. M. Humphrey
Department of Chemistry
The University of Texas at Austin
105 E. 24th Street Stop A5300, Austin, TX 78712, USA
E-mail: henkelman@utexas.edu; smh@cm.utexas.edu
H. Li
Advanced Institute for Materials Research (WPI-AIMR)
Tohoku University
Sendai 980–8577, Japan

[+]Present address: Department of Chemistry, Augsburg University, 700 21st Avenue S., Minneapolis, MN 55454, USA
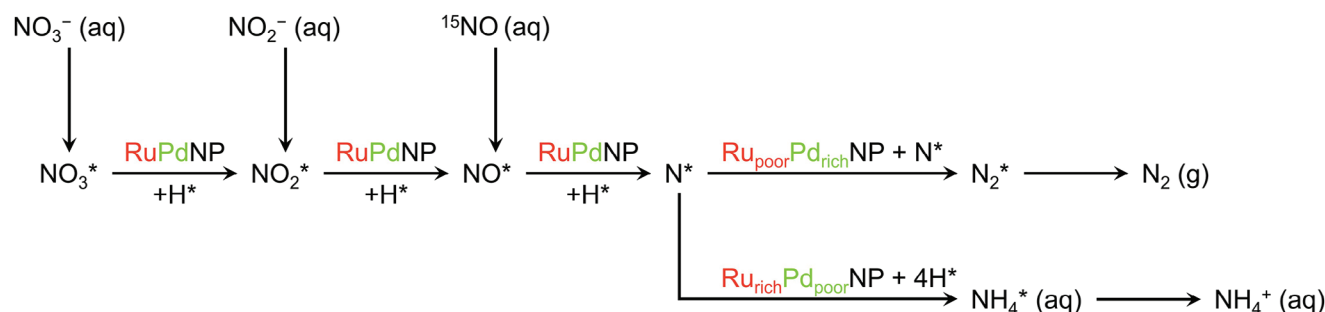
Scheme 1. Catalytic reaction pathways for NO_3^-, NO_2^-, and NO hydrogenation over RuPdNP catalysts. The * symbol represents adsorbed states. The end-product selectivity is determined by the divergent pathways stemming from adsorbed N which can either combine with another adsorbed N leading to N_2 or with adsorbed H to eventually yield NH_4^+.

US Environmental Protection Agency (USEPA) maximum contaminant level (MCL) of 10 mg-N L^{-1}.[25] High levels of agricultural NO_3^- pollution pose major environmental concerns due to increased eutrophication and hypoxia in surface waters. Simultaneously, energy is wasted in the manufacture of ammonia-based fertilizers via the energy-intensive Haber-Bosch process.[26–32] High levels of NO_3^- also pose a major public health risk to populations that rely on this water for drinking: NO_3^- can be reduced in vivo to nitrite (NO_2^-), which can cause methemoglobinemia and may react further to form potentially carcinogenic *N*-nitroso compounds. Implications of the latter include higher rates of various cancers with long-term exposure to even low levels of NO_3^- being shown to increase rates of various cancers.[33–36] Currently, the state-of-practice for NO_3^- removal from drinking water is ion exchange (IX). However, IX does not fully destroy NO_3^-, but merely transfers it from the finished water into a concentrated waste brine which requires further disposal or treatment. Additionally, IX requires large amounts of brine to regenerate exchange resins, resulting in high operating costs. Other methods (e.g., biological denitrification, reverse osmosis) have also been explored, but these strategies have their own drawbacks that hinder their implementation and as such are not the focus of this work.[37]

Both thermal catalytic and electrocatalytic reduction of NO_3^- have shown promise as potentially disruptive technologies for the direct removal of NO_3^- during water treatment by reduction of NO_3^- to create N_2 or NH_4^+. The first two steps of both processes are adsorption of NO_3^- to form $NO_3^-_{(ads)}$ and then the reduction of $NO_3^-_{(ads)}$ to $NO_2^-_{(ads)}$. Generally, the $NO_2^-_{(ads)}$ is then subsequently reduced to $NO_{(ads)}$, and then, through a series of intermediates to either N_2 or NH_4^+ (**Scheme 1**).[38–40] Typically during electrocatalysis, the reduction process occurs through direct electron transfer from the electrode to the adsorbed N-species. The competition of the various mechanisms during electrocatalytic NO_3^- reduction, which have been well summarized in a number of recent reviews, have a direct influence on the end-product selectivity. Traditionally, coinage metals (Cu, Ag, Au) and platinum-group metals (PGM; Rh, Ru, Ir, Pt, Pd) are used as cathodic materials for electrocatalytic NO_3^- reduction, though a number of other metals and metal oxides (e.g., Ti, TiO_2, Fe, Bi) have also been studied in an attempt to improve catalyst performance or to target certain end-products.[39,41,42] Some of these studies have shown that the mechanism of electrocatalytic NO_3^- reduction is highly dependent on the actual exposed facets of the metal elec-

trode, and exposing ideal facets can improve performance and alter selectivity.[43,44] Further, the addition of secondary metals has been used to improve activity during electrocatalytic NO_3^- and NO_2^- reduction and to direct end-product selectivity.[45–48] However, these studies have only explained why one end-product is more favored than another, and they have not yielded tunable end-product control. More recent work also suggests that while electrocatalytic and thermal catalytic NO_3^- reduction may follow similar pathways, there are major mechanistic differences between the two technologies, and the study of one should not exclude the other.[40,46,49]

In thermal catalysis, the reduction processes use atomic hydrogen as the electron donor. The atomic hydrogen is usually generated in situ by oxidative dissociation of H_2 using a PGM. The first step of transforming adsorbed NO_3^- to NO_2^- often requires the presence of a promoter metal (e.g., In, Cu, Sn) to help activate the first N–O bond in NO_3^-, and generally this step is not regarded as rate limiting for thermal catalysis.[50,51] Subsequently, NO_2^- migrates to the PGM where it is further reduced to NO, and then, through a series of intermediates, to N_2 or NH_4^+. The promoter is then regenerated by reduction with additional H_2.[6,51–55] Historically, Pd has been the preferred PGM for thermal catalysis (with In, Cu, or Sn as a promoter) due to its relatively high activity and its high selectivity for N_2.[52,56,57] Formation of NH_4^+ has commonly been avoided as it promotes bacterial growth in finished water; this negatively impacts the taste and odor of drinking water, and raises concerns regarding growth of pathogens.[58–60] However, NH_4^+ is a valuable product that can be re-used in agriculture, such that its recovery has more recently garnered attention. Alternatives to Pd-based catalysts (e.g., nickel phosphide (Ni_2P), ruthenium (Ru), etc.) have emerged as promising alternatives that can achieve near complete selectivity toward NH_4^+ formation upon NO_3^- reduction, and, importantly, they do not require a promoter metal for the first step of NO_3^- reduction to NO_2^-.[61,62] Unfortunately, Ni_2P catalysts can only activate NO_3^- in low pH environments (pH 2–4),[61] whereas, Ru-based catalysts show high activity for NO_3^- reduction at pH ranges closer to those of typical drinking water (e.g., 5.0–5.5).[62] Ru is also significantly less expensive than Pd ($14.95 g_{Ru}^{-1} versus $42.91 g_{Pd}^{-1}; MetalsDaily and APMEX, Inc.; August 2023). A clear mechanistic understanding of how Pd and Ru surfaces alter the binding energies of species involved in competing NO_3^- reduction pathways is notably absent in this arena. Having a detailed understanding of key catalyst structure-function relationships can help

**ADVANCED
SCIENCE NEWS**

www.advancedsciencenews.com

NANO · MICRO

small

www.small-journal.com

explain why certain catalyst compositions select for different end-products, and how reaction thermodynamics can be exploited to obtain desired ratios of N_2 to NH_4^+; to-date, these relationships remain poorly understood from a fundamental standpoint. Although mixed ratios of N_2 and NH_4^+ might not be desirable for most nitrate reduction applications, the ability to tune binding energies to obtain specific product mixtures would have much wider applications in industrial-scale catalysis.

The goal of this work is to explore structure-selectivity correlations in ruthenium-palladium nanoparticles ($Ru_xPd_{100-x}NPs$) as a function of catalyst composition, which can itself be dictated by synthetic design. We synthesized a series of $Ru_xPd_{100-x}NPs$ with target ratios that span the entire composition range, corresponding to $x = 10, 30, 50, 70,$ and 90, by adapting previously published methods [63] that utilize a convenient and scalable microwave (MW)-assisted synthetic approach.[64,65] We then characterized the resulting solid-solution nanoparticles using a variety of techniques, including powder X-ray diffraction (PXRD), transmission electron microscopy (TEM), scanning transmission electron microscopy with energy dispersive X-ray spectroscopy (STEM-EDS), X-ray photoelectron spectroscopy (XPS), and inductively coupled plasma optical emission spectrometry (ICP-OES). This structural information is combined with experimental model catalytic studies, which are able to provide kinetic information of NO_3^-, NO_2^-, and NO reduction as a function of Ru-Pd composition. Finally, we employed computational chemistry in the form of density functional theory (DFT) to elucidate the observed reactivity and to relate it to catalyst behavior as pertains to the most prevalent NO_3^- reduction pathways that result in selective formation of N_2 and NH_4^+.

All the $Ru_xPd_{100-x}NP$ catalysts studied in this work were found to display pseudo-first-order reaction rates for NO_3^-, NO_2^-, and NO reduction by H_2, and the apparent hydrogenation activity was found to be heavily dependent on both the catalyst composition and the starting reagents employed. Furthermore, we found that selectivity towards NH_4^+ is indeed tunable as a function of catalyst composition, driven by competitive binding between N-species and H_2 at various Ru-Pd surface ensembles, which are present in different frequencies based upon the specific Ru:Pd ratios. Through our combined experimental and theoretical work, we were able to explore the hypothesis, that: "intrinsic variations in reactivity and adsorption of various reaction species on different $Ru_xPd_{100-x}NP$ surfaces are responsible for the observed difference in end-product selectivity, as well as the difference in activity."

2. Experimental Results

2.1. Microwave Synthesis of RuPdNPs

Ruthenium-palladium nanoparticles with random, solid-solution structures and finely tunable Ru:Pd compositions ($Ru_xPd_{100-x}NPs$) were prepared by the co-reduction of common Ru^{3+} and Pd^{2+} salts using a microwave-assisted polyol method. The target value of x was determined based on the molar ratio of metal precursors employed in a given reaction, such that the total molar amount of metal (Ru + Pd) was 0.10 mmol in all cases (Table S1, Supporting Information). In general, a solution containing a specified molar ratio of $RuCl_3$ and K_2PdCl_4 was

dissolved in ethylene glycol (EG) and injected directly into a hot solution of EG containing excess poly(vinylpyrrolidone) (PVP) that was pre-heated to 185 °C, at a controlled rate, within a CEM MARS-5 microwave reactor. After heating for 30 min, the resulting PVP-capped RuPdNPs were isolated by precipitation (see the Experimental Methods section in the Supporting Information for details). ICP-OES revealed actual resulting compositions with $x = 83.9, 67.4, 45.6, 27.5,$ and 11.1, compared to the notional (target) compositions of $x = 90, 70, 50, 30,$ and 10, as shown in **Figure 1a**; Table S2 (Supporting Information). The uniformly close agreement between target and actual compositions across all Ru:Pd ratios indicates that Ru^{3+} and Pd^{2+} were successfully co-reduced under the chosen reaction conditions, without the co-formation of secondary, monometallic species. The lattice structures of the $Ru_xPd_{100-x}NPs$ were investigated using powder X-ray diffraction (PXRD). In their monometallic forms, Ru exhibits hexagonal close packing (*hcp*), while Pd resides in the face-centered cubic (*fcc*) lattice. Ru can be crystallized in a relatively stable, kinetic *fcc* setting in small nanoparticles,[66–68] and as such, it is known to readily adopt an *fcc* structure when alloyed with another *fcc* metal.[63,69,70] Interestingly, in this case, Figure 1b shows that the diffraction patterns of the samples revealed characteristics of both *hcp* and *fcc* lattice structures (Figure 1b). The extent to which one structure dominated over the other was dependent on the particle composition, such that Ru-rich particles displayed greater *hcp* character, while Pd-rich particles showed more *fcc* character, in agreement with previous reports.[63,71,72]

Transmission electron microscopy (TEM; Figure 1c–i) reveals quasi-spherical particles for all $Ru_xPd_{100-x}NPs$, contrary to previous reports of Ru-rich RuPdNPs which indicated elongated, non-spherical particles.[63] This difference in particle morphology could be due to capping agent effects from the higher PVP-to-metal ratio used in this work versus that of Kusada et al., and/or the presence of hotspots generated by the interaction of the microwave irradiation, in which early nanoparticle seeds could facilitate isotropic growth. In this work, as the atomic percent of Pd in the alloy was increased, the particle shape became more cuboctahedral, which is consistent with the equilibrium structure of *fcc* nanocrystals, such as pure PdNPs (Figure 1i).[73,74] As shown by Figure 1j, the size of the particles increases from monometallic RuNPs (2.6 nm) as the amount of Pd increased. The size reached a maximum at $Ru_{30}Pd_{70}NPs$ (8.4 nm) and then decreased to $Ru_{10}Pd_{90}NPs$ (8.0 nm) and again to monometallic PdNPs (5.6 nm). All compositions of $Ru_xPd_{100-x}NPs$ displayed narrow size dispersity ($\sigma < \pm20\%$).

Scanning transmission electron microscopy with energy dispersive X-ray spectroscopy (STEM-EDS) analyses were performed to confirm random alloying of Ru and Pd within the particles as opposed to a mix of RuNPs and PdNPs or a segregated structure; representative results of the $Ru_{50}Pd_{50}NPs$ are shown in **Figure 2**. Figure 2b–d show the maps of Ru, Pd, and their elemental overlays, respectively. Taken together, these maps give direct evidence of a solid-solution Ru-Pd structure, despite their classical immiscibility in bulk at room temperature.[75] EDS line scan analyses (Figure 2e,f) further corroborate solid-solution alloys within individual particles. STEM-EDS maps of various compositions (Figure S1–S4, Supporting Information) confirm that, on the nanoscale, Ru and Pd can be alloyed across the entire
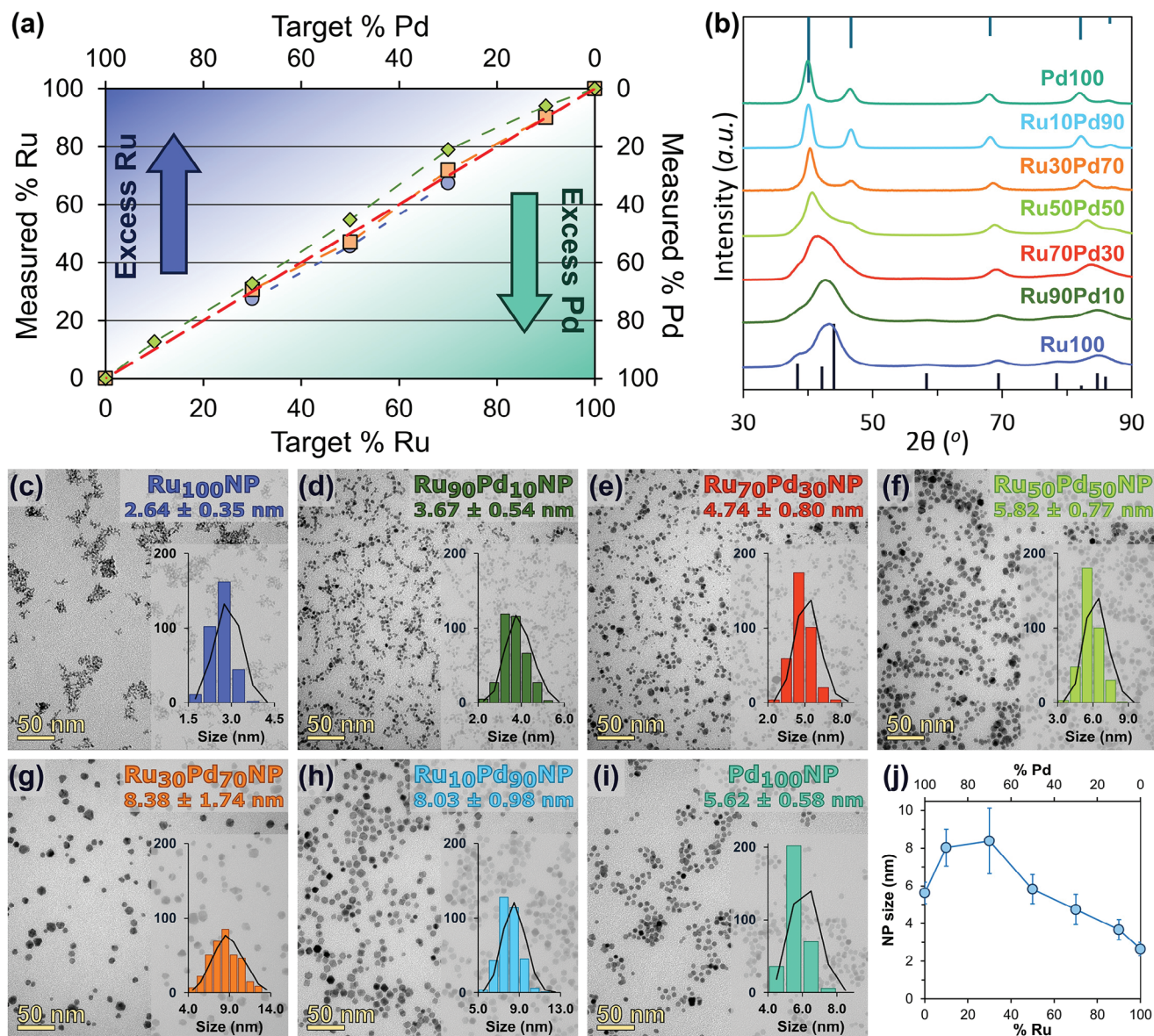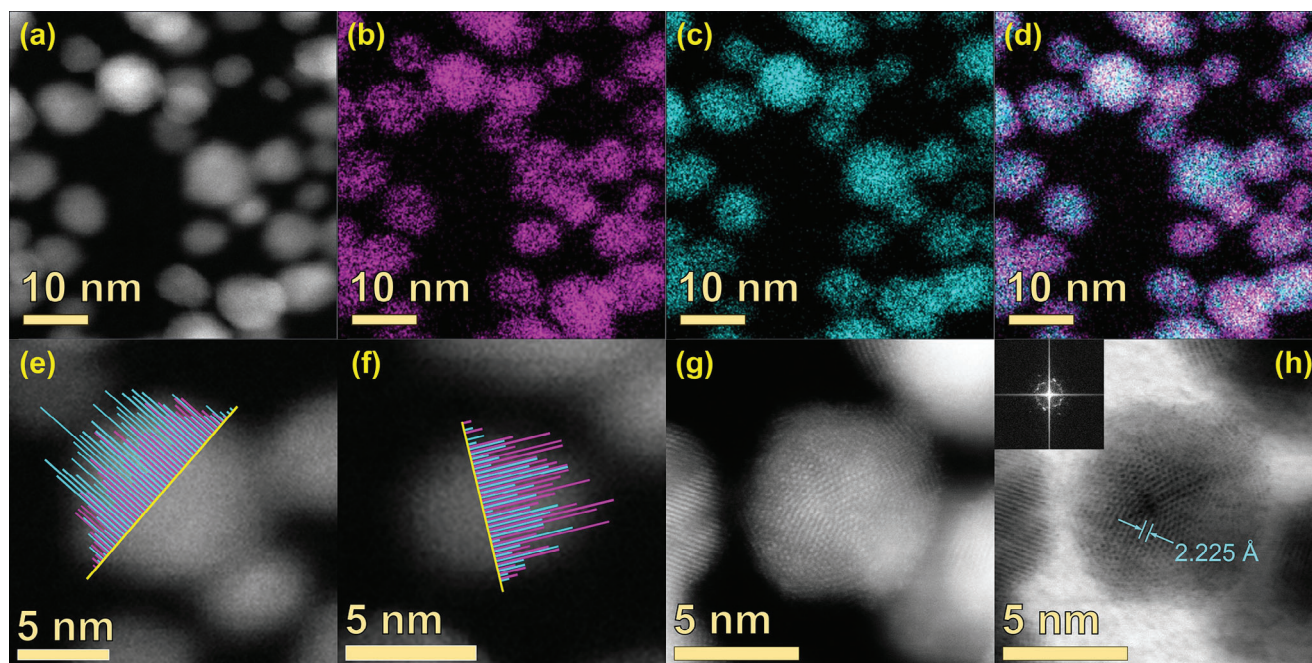
Figure 1. a) Comparison of measured nanoparticle compositions by different techniques versus the target composition (dashed red line): ICP-OES (blue circles), EDS (green diamonds), and XPS (orange squares). b) Powder X-ray diffraction patterns for Ru_xPd_{100-x}NPs. The vertical lines represent expected reflections for *hcp* Ru (black; from the bottom) and *fcc* Pd (teal; from the top). Representative low-resolution TEM images for c) RuNPs, d) $Ru_{90}Pd_{10}$NPs, e) $Ru_{70}Pd_{30}$NPs, f) $Ru_{50}Pd_{50}$NPs, g) $Ru_{30}Pd_{70}$NPs, h) $Ru_{10}Pd_{90}$NPs, and i) PdNPs. The insets show size distributions with histograms of measured sizes. Scale bars shown are 50 nm. j) Relationship between particle composition and particle size for Ru_xPd_{100-x}NPs.

composition range. The composition results from EDS analysis yield values of $x = 94.1, 78.9, 54.7, 32.8$, and 12.6, in relatively close agreement with values calculated from ICP (Figure 1a; Table S2, Supporting Information). STEM analyses of the monometallic RuNPs and PdNPs show that both monometallic samples consisted of single crystalline particles (Figure S5 and S6, Supporting Information, respectively). Analysis of the RuNPs yields a lattice d-spacing of 2.061 Å, closely corresponding to the ⟨101⟩ planes of pure *hcp* Ru (expected d-spacing of 2.055 Å). Analysis of the monometallic PdNPs yields a d-spacing of 2.247 Å, which agrees with the expected d-spacing of the ⟨111⟩ planes of pure *fcc* Pd (2.246 Å). The STEM images of the alloys show that

the alloyed particles were polycrystalline with small domains (see Figure 2g,h, Figure S7–S10, Supporting Information). For particles with x ≤ 50, the measured d-spacing corresponds to the *fcc* ⟨111⟩ planes, with the measured d-spacing decreasing with increasing Ru content (x). The measured d-spacing of $Ru_{70}Pd_{30}$NPs and $Ru_{90}Pd_{10}$NPs corresponds well to what was expected for *hcp* ⟨002⟩ planes, and the measured d-spacings again decrease with increasing Ru content (x). Our results are in close agreement with previous reports of alloyed RuPdNPs that have demonstrated that individual particles consist of small *hcp* and *fcc* domains.[63]

The surface and near subsurface compositions of the Ru_xPd_{100-x}NPs were assessed by X-ray photoelectron

**ADVANCED
SCIENCE NEWS**

www.advancedsciencenews.com

**NANO · MICRO
small**

www.small-journal.com

Figure 2. a) HAADF-STEM image, b) Ru-L EDS map, c) Pd-L EDS map, and d) Ru-Pd overlay of several $Ru_{50}Pd_{50}NPs$. Scale bars shown are 10 nm. e,f) Compositional EDS line profiles for Ru (purple) and Pd (cyan) for single $Ru_{50}Pd_{50}NPs$. Scale bars shown are 5 nm. g) HAADF-STEM image and h) corresponding BF-STEM image of a single $Ru_{50}Pd_{50}NP$. Scale bars shown are 5 nm. Shown in h is the measured lattice d-spacing of 2.225 Å, which corresponds to the *fcc* ⟨111⟩ planes of the $Ru_{50}Pd_{50}NPs$. The inset in h shows the forward Fourier transform (FFT) calculated from the NP.

spectroscopy (XPS), where the X-ray penetration depth was somewhat selective to the NP exteriors. These data are in good agreement with both the target nominal compositions and the corresponding compositions measured by ICP-OES and EDS (Figure 1a; Table S2, Supporting Information). In direct agreement with elemental mapping studies, Ru surface enrichment was not observed, despite the difference in reduction potentials of the two metals: $E_{Ru} = 0.60$ V versus $E_{Pd} = 0.95$ V.[76] The lack of an observed surface Ru bias is likely due to the presence of PVP overlayers; previous studies have demonstrated that adsorbates such as H [77] and N [6] can stabilize Pd atoms at NP surfaces. XPS was also used to examine the distribution of average oxidation states of surface atoms, which were exposed to air during synthesis and storage and were therefore assumed to be oxidized to a greater extent than when under reducing catalytic conditions (Figure S11–S13, Supporting Information). The subsurface Ru and Pd atoms are expected to be zero-valent since they are fully coordinated with other metal atoms. The Ru 3p peaks were chosen for analysis due to the superimposition and resulting convolution of the Ru 3d region with the C 1s region (Figure S12, Supporting Information). For all Ru-containing samples, the Ru atoms at the particle surface were present as Ru^0, with the Ru $3p_{3/2}$ peak appearing at 461.7 eV (Table S3, Supporting Information; *cf.* 461.20–461.70 eV).[78,79] XPS analysis revealed a combination of Pd^0 and Pd^{2+} for all Pd-containing catalysts, with Pd $3d_{5/2}$ peaks at 335.3 eV and 337.0 eV for Pd^0 and Pd^{2+}, respectively. The Pd $3d_{3/2}$ peaks appear approximately 5.3 eV higher than the Pd $3d_{5/2}$ peaks (Table S4, Supporting Information). Generally, ≈25% of the Pd surface atoms were present in the Pd^{2+} oxidation state for all compositions (Table S5, Supporting Information); this was in direct opposition to prior

work with Pd-based alloys where the fraction of Pd^{2+} decreased as the amount of Pd in the alloy decreased.[80–82] However, it was anticipated that surface oxidation should not impact catalyst performance, since the catalysts require pre-reduction under flowing H_2 gas, so all exposed metal surfaces should be reduced to their metallic, zero-valent state.[83]

2.2. Catalytic Nitrate Reduction

The as-synthesized $Ru_xPd_{100-x}NPs$, RuNPs, and PdNPs were supported on amorphous silica (a-SiO_2) via direct deposition from aqueous-organic suspensions, with notional targeted metal loadings of 4–5 wt% (Ru + Pd). ICP-OES analysis of the supported catalysts confirmed successful loading of all RuPdNP compositions on a-SiO_2, with actual loadings between 3.8–4.7 wt% (Table S6, Supporting Information). Analyses of the supported particles by TEM demonstrated no change in particle morphology during the deposition process (Figure S14, Supporting Information). Further, STEM-EDS analysis of SiO_2-supported $Ru_{50}Pd_{50}NPs$ after catalysis (Figure S15, Supporting Information) confirmed the stability of the NPs on the SiO_2 support, and showed that the atomic structure of the NPs was stable throughout both deposition and catalysis. Amorphous SiO_2 was chosen here as the catalyst support because it is relatively inert and thus should not play a role in the measured catalytic activity or selectivity, allowing for examination of the intrinsic structure-function relationship of RuPdNPs.[84,85] Catalytic reduction experiments using NO_3^- were performed in semi-batch reactors using H_2 gas as the reducing agent. For NO_3^- reduction, all catalysts displayed pseudo-first-order kinetics (Figure S16, Supporting
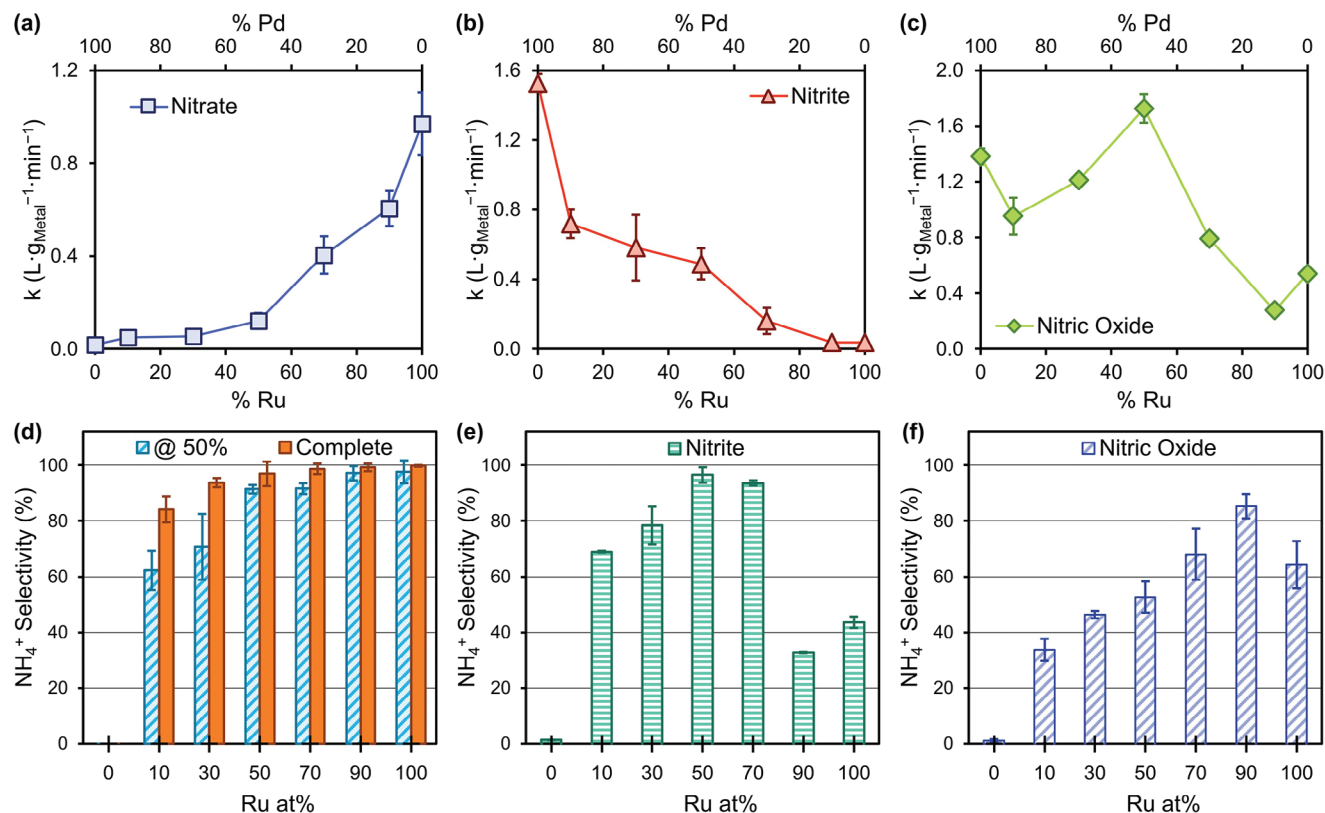
Figure 3. First-order rate constants for a) aqueous NO_3^- reduction, b) aqueous NO_2^- reduction, and c) aqueous ^{15}NO reduction normalized to total metal (i.e., Ru + Pd) as wt% of catalyst in units of liters per gram metal per min. NH_4^+ selectivity (as a fraction of mol NH_4^+ produced per mol N lost) at d) 50% conversion (blue striped bars) and complete conversion of initial NO_3^- (orange solid bars), e) complete conversion during NO_2^-, and f) complete conversion during ^{15}NO reduction.

Information), from which apparent first-order rate constants were calculated (Table S7, Supporting Information). These rate constants were then normalized to the total amount of metal in each catalyst as shown in **Figure 3**a–c. These rate constants were further normalized to turnover frequencies (TOFs; Figure S17a, Supporting Information), and the trends in activity between the mass-normalized activity and the TOFs were in good agreement.

The catalytic activity of Ru_xPd_{100-x}NPs in NO_3^- reduction was found to have a direct correlation with the value of x: as the amount of Ru in the catalyst decreased, the NO_3^- activity also decreased. The monometallic RuNP-SiO$_2$ catalyst displayed the highest metal-normalized activity of 0.97 L g$_M^{-1}$ min^{-1}, several times lower than reported by Huo et al. (cf. 4.13 L g$_M^{-1}$ min^{-1}).[62] This difference may reflect the different reaction conditions used here versus those used by Huo and coworkers, or intrinsic reactivity differences that stem from the different preparation methods of the RuNPs in that work and ours. The monometallic PdNP-SiO$_2$ catalyst displayed very little degradation of NO_3^-, with a calculated activity of 0.01 L g$_M^{-1}$ min^{-1}; this was in good agreement with other studies using Pd-based catalysts for NO_3^- reduction.[52,57,86,87] The decreasing activity of the alloyed Ru_xPd_{100-x}NP-SiO$_2$ catalysts with decreasing amount of Ru present was due to the limited ability of Pd to abstract the first oxygen from NO_3^- to initiate the reaction. The estimated Damkohler coefficient (Da) was <<1 for the least active catalyst

($Ru_{10}Pd_{90}$NP-SiO$_2$), indicating that external mass transfer limitations of NO_3^- and H$_2$ on the reactions were negligible; similarly, the Weisz-Prater parameter (C$_{WP}$) was <<1, indicating that internal mass transfer within the SiO$_2$ pores did not limit the overall reaction rates (see Supporting Information for details on the calculations of both parameters).

The end-product selectivity of the Ru_xPd_{100-x}NP-SiO$_2$ catalysts was assessed at both 50% loss and complete loss of NO_3^- (Figure 3d and **Table 1**). In both instances, the selectivity for NH_4^+ decreased as the amount of Ru in the catalyst (x) was

Table 1. Selectivity of NH_4^+ versus N_2 (as % NH_4^+) during NO_3^-, NO_2^-, and NO hydrogenation over Ru_xPd_{100-x}NP-SiO$_2$ catalysts.

Ru:Pd	NO_3^- reduction[a]	NO_3^- reduction[b]	NO_2^- reduction[b]	NO reduction[b]
100:0	97.6 (4.2)	99.8 (0.3)	43.7 (2.0)	64.3 (8.5)
90:10	97.1 (2.6)	99.2 (1.4)	32.7 (0.2)	85.3 (4.3)
70:30	91.6 (1.9)	98.7 (1.9)	93.6 (0.9)	68.0 (9.2)
50:50	91.4 (1.5)	96.9 (4.4)	96.5 (2.8)	52.7 (5.6)
30:70	70.8 (11.8)	93.7 (1.6)	78.4 (6.8)	46.3 (1.3)
10:90	62.3 (7.0)	84.1 (4.7)	68.9 (0.3)	33.7 (3.9)
0:100	–	–	1.4 (0.1)	1.2 (0.4)

[a] Measured at 50% loss of NO_3^-; [b] Measured at 100% loss of N-parent species. Values in parentheses represent standard deviation of measurements.

**ADVANCED
SCIENCE NEWS**

www.advancedsciencenews.com

**NANO · MICRO
small**

www.small-journal.com

decreased. The NH_4^+ selectivity of the catalysts increased as NO_3^- conversion approached complete conversion. This was likely due to the decreasing concentration of NO_3^- in solution, which was anticipated to decrease the N:H ratio on the catalyst surface, thus making the formation of N–H bonds more likely.[54,88–90] Supported nanoparticle catalysts with intermediate or higher amounts of Ru displayed > 90% selectivity towards NH_4^+ even at 50% reduction of NO_3^-; in contrast, more Pd-rich catalysts displayed significantly less NH_4^+ selectivity (70.8% and 62.3% for $x = 30$ and 10, respectively).

2.3. Nitrite and NO as Reduction Intermediates

The current mechanistic understanding of NO_3^- reduction by noble metal catalysts indicates that NO_3^- is first reduced to NO_2^-, which is further reduced to NO, then transformed to N, which can ultimately lead to either NH_4^+ formation by reaction with nearby H atoms or N_2 formation by direct reductive elimination.[51,62,86,91,92] In this study, neither NO_2^- nor NO was detected during NO_3^- reduction, indicating that the reduction of both species was faster than their formation under the measured conditions or they were strongly sorbed. To better understand the impact of both species on the selectivity of NO_3^- reduction, reactions were performed with either NO_2^- or NO as the initial N-species.

When reactions were initiated using NO_2^-, all catalysts again displayed pseudo-first-order kinetics from which apparent first-order rate constants were calculated before being normalized to the total metal content (Figure S18 and Table S7, Supporting Information) and to TOFs (Figure S17b, Supporting Information). The activity of Ru_xPd_{100-x}NPs for NO_2^- reduction decreased as the amount of Ru in the catalyst (x) increased (Figure 3b). This trend was in direct opposition to that seen when NO_3^- was the initial reactant species. The monometallic PdNP-SiO$_2$ catalyst displayed the highest activity of 1.53 L g$_M^{-1}$ min^{-1} (cf. 1.3 L g$_M^{-1}$ min^{-1} from Hörold et al.,[52] 1.35 L g$_M^{-1}$ min^{-1} from Troutman et al.,[82] and 2.0 L g$_M^{-1}$ min^{-1} from Seraj et al.[80]). Only ≈15% of the NO_2^- was degraded after three hours when using the pure RuNP-SiO$_2$ or $Ru_{10}Pd_{90}$NP-SiO$_2$ catalysts ($k = 0.036$ L g$_M^{-1}$ min^{-1} for both). This trend agrees with previous reports, where the NO_2^- reduction activity on Ru-catalysts was much lower than Pd-catalysts.[62] Selectivity behavior of the Ru_xPd_{100-x}NP-SiO$_2$ catalysts during NO_2^- reduction was completely different than the selectivity during NO_3^- reduction (Figure 3e and Table 1). In agreement with previous reports, the PdNP-SiO$_2$ catalyst displayed almost complete selectivity for N_2 gas (98.6% N_2), while the RuNP-SiO$_2$ catalyst yielded a mix of NH_4^+ and N_2 (43.7% NH_4^+ versus 56.3% N_2).[62,80,82] All alloy catalysts except $Ru_{10}Pd_{90}$NP-SiO$_2$ displayed higher selectivity towards NH_4^+ than the pure RuNP-SiO$_2$ catalyst. The $Ru_{50}Pd_{50}$NP-SiO$_2$ displayed near-complete selectivity towards NH_4^+, closely followed by $Ru_{70}Pd_{30}$NP-SiO$_2$ (96.5% NH_4^+ and 93.6% NH_4^+, respectively).

When reactions were initiated using ^{15}NO, all catalysts displayed pseudo-first-order kinetics and demonstrated near-complete (≥ 90%) reduction of all ^{15}NO (Figure S19 and Table S7, Supporting Information). The ^{15}NO reduction activity of the Ru_xPd_{100-x}NP-SiO$_2$ displayed a volcano-shaped dependence on
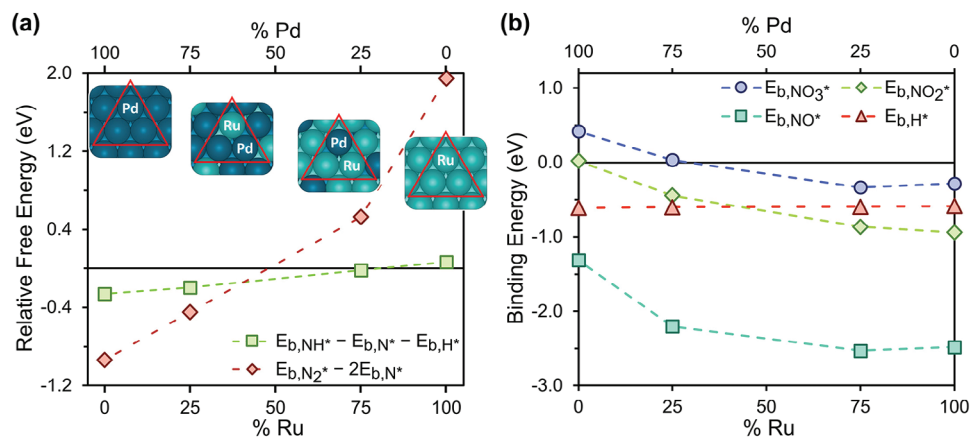
composition (Figure 3c; Figure S17c, Supporting Information), in contrast with both NO_3^- and NO_2^- reduction activity. The pure PdNP-SiO$_2$ catalyst outperformed the pure RuNP-SiO$_2$ (1.34 L g$_M^{-1}$ min^{-1} versus 0.55 L g$_M^{-1}$ min^{-1}, respectively). Upon incorporation of a small amount of secondary metal (e.g., $Ru_{90}Pd_{10}$NPs and $Ru_{10}Pd_{90}$NPs), the activity was markedly decreased. The $Ru_{50}Pd_{50}$NP-SiO$_2$ catalyst displayed the highest ^{15}NO reduction activity of 1.80 L g$_M^{-1}$ min^{-1}. The selectivity behavior of the Ru_xPd_{100-x}NP-SiO$_2$ catalysts is similar to that during NO_3^- reduction: generally, as the amount of Ru in the alloy (i.e., the value of x) increases the catalyst becomes more selective for NH_4^+ formation (Figure 3f and Table 1). The pure PdNP-SiO$_2$ catalyst displayed very little NH_4^+ formation during ^{15}NO reduction (1.2%), in agreement with previous studies looking at NO reduction using a Pd catalyst, which found that Pd catalysts display high (> 90%) N_2 selectivity.[93] When a small amount (e.g., 10%) of Ru was added to the catalyst, the NH_4^+ selectivity increased to 33.7%. The selectivity steadily increased to reach that of the $Ru_{90}Pd_{10}$NP-SiO$_2$ catalyst (85.3% NH_4^+). However, the pure RuNP-SiO$_2$ notably did not follow this trend; instead, ^{15}NO reduction over the RuNP-SiO$_2$ resulted in a mixture of both $^{15}NH_4^+$ and $^{15}N_2$ gas (64.3% $^{15}NH_4^+$ and 35.7% $^{15}N_2$).

3. Computational Results

As mentioned above, selectivity can be controlled either by changing the reaction conditions (i.e., pH, H_2 gas flow rate) or by changing the intrinsic reactivity via composition/structure tuning (resulting in the control of relative barrier heights). It is well documented that both pH and H_2 flow rate play a major role in both NO_3^- removal activity and selectivity towards NH_4^+ versus N_2 when using Pd-based catalysts.[52,89,92] Ru-catalysts have also shown pH-dependent NO_3^- reduction activity, although the catalytic selectivity remained high (> 90%) at all tested pH values (pH 3–10).[62] Additionally, all NO_3^- reduction experiments in this work were well buffered (pH = 6.4 ± 0.2) and were performed with the same H_2 flow rate. Therefore, neither the pH nor the H_2 flow were expected to cause the observed selectivity differences of the alloy catalysts.

We hypothesize that the observed difference in end-product selectivity, as well as the differences in activity, are due to variations in intrinsic reactivity and adsorption of various reaction species on the different Ru_xPd_{100-x}NP surfaces. This infers that, when reactivity dominates, the observed selectivity is primarily determined by the thermodynamics of the competing pathways for N-species reduction. By comparison, when surface coverage effects are dominant, the product selectivity is controlled by the ratio of adsorbed N versus H species that are co-adsorbed on the nanoparticle surfaces, which determines whether N–H or N–N bond formation is more likely (regardless of potential differences in the relative energies of the competing pathways). To evaluate our hypothesis, we used DFT to calculate the adsorption free energies of key reaction species (e.g., NO_3^-, NO_2^-, NO, N, H, NH, and N_2) on various Ru_xPd_{100-x} surfaces and to calculate the energetics related to NH_4^+ and N_2 formation, shown in **Figure 4**. We were thus able to examine how the thermodynamics of the competing pathways for NH_4^+ formation and N_2 formation, as

**ADVANCED
SCIENCE NEWS**

www.advancedsciencenews.com

NANO · MICRO
small

www.small-journal.com

Figure 4. a) Energy requirement to move from the N*, H* stage to the NH* stage (green squares) or from the 2N* stage to the N_2* stage (red diamonds) on a Ru_{100}, $Ru_{75}Pd_{25}$, $Ru_{25}Pd_{75}$, and Pd_{100} surface. The more favorable pathway is the one with a lower relative free energy for each composition. The insets show the four possible representative triatomic ensembles on the alloy surface: Ru_3, Ru_2Pd_1, Ru_1Pd_2, and Pd_3. b) Comparison of the binding energies of nitrate (NO_3*; blue circles), nitrite (NO_2*; green diamonds), nitric oxide (NO*; teal squares), and hydrogen (H*; red triangles) on various Ru_xPd_{100-x} surfaces.

well as surface coverage effects, impact selectivity during NO_3^-, NO_2^-, and NO reduction over RuPdNP surfaces.

3.1. Thermodynamics of Competing NH_4^+ versus N_2 Formation Pathways on RuPd Surfaces

Previous theoretical studies have demonstrated that the hydrogenative reduction of NO_3^- follows a single pathway to the formation of adsorbed NO (i.e., NO*, where "*" represents an adsorbed state), before splitting into the pathways leading to NH_4^+ or N_2.[54,62] Here, using DFT calculations, we calculated binding energies of the NO*, N*, H*, NH*, and N_2* species on Ru_xPd_{100-x}NP catalysts to better understand the end-product tunability of reaction selectivity during NO_3^- reduction (Scheme 1). The relative free energies of the different reaction steps were calculated on four different Ru_xPd_{100-x}NP surfaces (Ru_{100}, $Ru_{75}Pd_{25}$, $Ru_{25}Pd_{75}$, and Pd_{100}). For alloy surfaces, the overall adsorbate binding energy was calculated by taking a weighted average of the adsorbate binding energies at each of the possible triatomic ensembles (Table S8, Supporting Information). The results indicate that the most important step in determining selectivity is the progression from N* to either NH* or N_2* (i.e., forming an N–H bond from N* and H* or forming an N–N bond from two adsorbed N*). Thus, comparing the N–H bond formation energy with the N–N bond formation energy may be a good descriptor of catalyst selectivity, where the lower formation energy (i.e., a more negative value meaning more exothermic or a less positive value meaning less endothermic) will be more favorable. These results are shown in Figure 4a, where the difference in binding energies of States 2 and 1 are plotted as a function of catalyst composition (for example [$E_{b,NH*}$ − $E_{b,N*}$ − $E_{b,H*}$] as shown by the green squares and [E_{b,N_2*} − $2E_{b,N*}$] as shown by the red diamonds); the values used are presented in Table S9 (Supporting Information). DFT calculations show that N* strongly binds to the pure Ru catalyst surface, and so both N–H and N–N formation are endothermic. On monometallic Ru_{100} catalysts, N–H formation requires 0.06 eV, which is much less than the
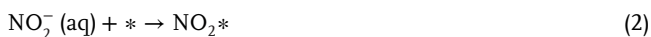
1.95 eV required for N–N formation. Thus, the formation of N–H, and eventually NH_4^+, is thermodynamically favored on a Ru_{100} catalyst. As the fraction of Ru in the catalyst decreases, the N binding energy becomes weaker (more positive), and the difference between the N–H bond formation energy and the N–N bond formation energy also decreases. Correspondingly, a $Ru_{75}Pd_{25}$ surface is still predicted to favor N–H formation over N–N (−0.02 eV versus 0.53 eV, respectively). However, in the other extreme, the energy for N–N formation at a $Ru_{25}Pd_{75}$ nanoparticle surface is predicted to become slightly more favorable than N–H formation (−0.45 eV versus −0.19 eV), indicating a change in overall selectivity as the amount of Pd in the catalyst increases. On a pure Pd_{100} surface, N* binds weakly compared with NH* and N_2* so both N–H and N–N formation are exothermic. N–N formation is much more exothermic than N–H formation (−0.94 eV versus −0.26 eV, respectively) meaning N_2 is expected to be the primary product using a pure Pd catalyst.

3.2. Surface Coverage Effects from the Adsorption of H, NO_3^-, NO_2^-, and NO

It is important to note that the calculations in Section 3.1 do not take into consideration surface coverage effects, and therefore only represent the thermodynamically favored end-product formation. We postulate that the selectivity of Ru_xPd_{100-x}NP catalysts during NO_3^-, NO_2^-, and NO reduction may be impacted by, if not controlled by, the competitive adsorption of NO_3^-, NO_2^-, NO, and H_2. For example, it has been proposed that increasing initial NO_2^- concentrations during reduction over pure Ru and Pd catalysts leads to decreasing activity because the NO_2^- outcompetes the H_2 for adsorption onto the catalyst surface, which limits the overall reaction.[62,94] To understand how NO_3^- and NO_2^- adsorption impact selectivity during reduction starting with each of these species, we calculated the binding energies of aqueous nitrate, nitrite, NO, and H on a pure Ru_{100} surface, a $Ru_{75}Pd_{25}$ surface, a $Ru_{25}Pd_{75}$ surface, and a pure Pd_{100} surface, shown in Figure 4b; Table S10 (Supporting Information),

**ADVANCED
SCIENCE NEWS**

www.advancedsciencenews.com

NANO · MICRO

small

www.small-journal.com

following reactions 1–4. These binding energies can influence the surface coverage of N- and H-species (and thus the N:H ratio on the surface), which in turn influences the catalyst activity and selectivity.

$$NO_3^- \, (aq) + * \rightarrow NO_3* \tag{1}$$

$$NO_2^- \, (aq) + * \rightarrow NO_2* \tag{2}$$

$$NO \, (aq) + * \rightarrow NO * \tag{3}$$

$$\frac{1}{2}H_2 \, (aq) + * \rightarrow H * \tag{4}$$

3.2.1. Hydrogen Binding

Previous computational studies of nitrite reduction over metallic catalysts have demonstrated that N binding on a metal surface is often a key descriptor in catalyst activity and selectivity, and that H binding energy, while important, is not a key determinant in reactivity or selectivity for catalytic NO_2^- reduction.[6] Our work here confirms this trend. Shown in Figure 4b by the red triangles, the overall difference in H binding between a pure Ru *fcc* (111) surface and a pure Pd *fcc* (111) surface is relatively small (−0.59 eV versus −0.61 eV, respectively). Additionally, it should be noted that the H binding using several pure Ru *hcp* slabs is also similar (approximately −0.6 eV). Further, our calculations show that alloying Ru and Pd does not significantly impact the H binding energy (Table S10, Supporting Information), which is reasonable, since both Ru and Pd have a high proficiency for dissociative hydrogen activation.[95,96] When compared to the binding energy trends of nitrogen-containing species, the relative consistency of H binding indicates that while H binding to the catalyst surface is important, dissociative H_2 binding alone is not a key determining factor for overall selectivity. This is further evidenced by the experimental setup: in all cases the experimental system is pre-sparged with hydrogen gas so that the catalyst surface is anticipated to be covered with a layer of adsorbed H* atoms when the NO_3^-, NO_2^-, or NO is introduced.

3.2.2. Comparison of Nitrate, Nitrite, and NO Binding Energies to H

Figure 4b shows that NO_3^- (blue circles) binds weaker to all catalysts than H (red triangles), indicating that NO_3^- should not outcompete H for available surfaces sites and nitrate reduction is not limited by a lack of H* atoms on the catalyst. On Pd-rich surfaces (pure Pd_{100} and $Ru_{25}Pd_{75}$) the nitrate binding energy is positive (0.42 eV and 0.03 eV, respectively) indicating a weak binding, so nitrate is unable to bind to the catalyst surface or binds very weakly, resulting in negligible nitrate reduction activity for Pd-rich catalysts on the extreme end of the composition range and low activity for intermediate Pd-rich catalysts ($Ru_{30}Pd_{70}$NPs). On Ru-rich surfaces (pure Ru_{100} and $Ru_{75}Pd_{25}$), nitrate binding energy is favorable (negative) but weaker than H binding (−0.28 eV on Ru_{100} and −0.33 eV on $Ru_{75}Pd_{25}$). Thus, NO_3^- can bind to surface sites to initiate reduction, but a relatively high H* coverage is expected which contributes to the good performance of Ru-rich catalysts for reducing nitrate. Hence, Ru-rich catalysts have

higher activity for NO_3^- reduction than catalysts with a moderate or low amount of Ru.

As shown in Figure 4b, NO_2^- (green diamonds) binds more strongly to a pure Ru_{100} surface (−0.94 eV) and a $Ru_{75}Pd_{25}$ surface (−0.86 eV) than H (red triangles). This strong binding can poison the catalyst surface with nitrite species leading to both decreased activity and NH_4^+ selectivity due to a lack of H* atoms (resulting in a high N:H ratio). On the other hand, nitrite binds weaker to a pure Pd_{100} surface (0.02 eV) and a $Ru_{25}Pd_{75}$ surface (−0.44 eV) than H, resulting in more H* atoms on the surface to carry out nitrite reduction. Interestingly, Figure 4b also reveals that NO (teal squares) binds much more strongly than H. NO binding is weakest on a pure Pd_{100} surface (−1.32 eV) and increases once Ru is introduced. NO binding is strongest on the $Ru_{75}Pd_{25}$ surface (−2.53 eV), and only slightly weaker on a pure Ru_{100} surface (−2.48 eV). This suggests that NO should strongly outcompete H for available surface sites, effectively poisoning the catalysts and leading to low NO reduction activity, similar to what is predicted for NO_2^-. However, this is not observed experimentally. We believe this is because NO was introduced as a gas, which introduces gas-to-liquid phase mass transfer limitations that experimentally limit the adsorption of NO to the catalysts, thereby lowering the N:H ratio on the catalyst surface. This limitation of NO adsorption results in higher apparent NO reduction activity.

4. Discussion

4.1. Selectivity During NO_3^- and NO Reduction is Primarily Controlled by Thermodynamics

Our experimental results for NO_3^- reduction, where NH_4^+ is predominantly formed by Ru-rich catalysts, and N_2 is formed in significant amounts only when the Ru composition is < 50% (Figure 3d) are in good agreement with the thermodynamic behavior of NH_4^+ and N_2 production as calculated by DFT (Figure 4a). At 50% loss of nitrate, all Ru-rich catalysts (i.e., $x \geq$ 50) displayed over 90% selectivity for NH_4^+ production. Based on our DFT results, the formation of N–H from adsorbed N and adsorbed H is much more favorable than N–N formation on these catalysts. Additionally, the surface coverage effects contribute to the NH_4^+ selectivity. The relatively weak binding of NO_3^- as compared to H will mean there is a relatively low N:H ratio on the surface making N–H formation statistically more likely to occur. Thus, both thermodynamics and surface coverage result in high NH_4^+ selectivity during NO_3^- reduction on Ru-rich catalysts. As we shift to more Pd-rich catalysts (i.e., $x < 50$), the selectivity for NH_4^+ at 50% loss of NO_3^- decreases and N_2 is produced in appreciable amounts (29.2% N_2 for $Ru_{30}Pd_{70}$NPs and 37.7% N_2 for $Ru_{10}Pd_{90}$NPs), though the majority of the end-product is still NH_4^+. The relatively weak NO_3^- binding (0.03 eV) on a Pd-rich surface indicates that though NO_3^- will adsorb to these surfaces, it is difficult to do so. This weak binding will result in a low N:H ratio on the catalyst surface, and the abundance of H atoms and lack of N atoms make N–H formation more likely than N–N formation, even though N–N is thermodynamically favored. Note that since a pure Pd catalyst cannot reduce NO_3^- on its own, we cannot compare selectivity experiments with our theoretical calculations for NO_3^- reduction. When we look at

selectivity at complete conversion of nitrate, we see a similar trend as at 50% loss of nitrate. All of the Ru-rich catalysts again show near-complete selectivity for NH_4^+ production (> 95%), and even the $Ru_{30}Pd_{70}$NPs show 93.7% selectivity for NH_4^+. As we approach complete conversion of NO_3^- using $Ru_{30}Pd_{70}$NPs, the surface coverage effects become even more important. Previous work by Zhao, et al. demonstrated that as hydrogenation approaches full conversion, the ratio of adsorbed N:H becomes even lower than at initial stages of reaction.[55] This decreasing N:H ratio further emphasizes the surface coverage effects, making N–H formation even more likely to occur, especially since both N–N and N–H formation are exothermic on Pd-rich surfaces. Thus, the NH_4^+ selectivity of all the catalysts increases as NO_3^- reduction approaches complete conversion, and more so for the Pd-rich catalysts than the Ru-rich catalysts.

Generally, the selectivity behavior of Ru_xPd_{100-x}NPs during NO reduction (Figure 3f) follows that of NO_3^- reduction (Figure 3d). Despite the very strong binding energies of NO, the adsorption of NO to the catalyst surface is limited by mass transfer from the gas phase to the aqueous phase, and so thermodynamics typically dominate the selectivity. Throughout the entire range of alloy compositions, as the amount of Ru increases, the NH_4^+ selectivity increases following the trend of N–N formation being more favored than N–H formation on Pd-rich surfaces but switching to N–H formation being more favored on Ru-rich surfaces. However, drawing firm conclusions about selectivity behavior is difficult because of the problems that arise from the NO feedstock being introduced as a gas, versus an aqueous species like NO_3^-.

4.2. Selectivity During NO_2^- Reduction is Controlled by both Thermodynamics and Surface Coverage Effects

While the selectivity behavior of Ru_xPd_{100-x}NPs during NO_3^- is well explained by NH* and N_2* formation, there is a deviation between the selectivity during NO_2^- reduction (Figure 3e) and the thermodynamics of the formation pathways. This deviation stems from the surface coverage effects demonstrated by the binding energies of NO_2^- and H. As mentioned above, the activities of the Ru_xPd_{100-x}NPs during NO_2^- are also controlled by NO_2^- and H binding. For pure Ru and very Ru-rich surfaces, NO_2^- binds more strongly than H. This strong NO_2^- binding poisons the catalyst surface, slowing activity. Additionally, because the NO_2^- outcompetes the H for available surface sites, there is a very high ratio of N:H on the catalyst surface for Ru-rich catalysts. Thus, even though the thermodynamics would favor N–H formation, the lack of available adsorbed H means that N–N formation is more likely on the Ru-rich surfaces. When we look at the behavior of the $Ru_{90}Pd_{10}$NPs, this is exactly what we see: 32.7% selectivity for NH_4^+. However, as we shift to more intermediate compositions (i.e., $x = 50$ and 70), the binding energy of NO_2^- becomes weaker while the binding energy of H stays relatively constant. Thus, NO_2^- does not as strongly outcompete H for available surface sites, and so the effect of surface coverage decreases and the effect of thermodynamics increase. Thus, the NH_4^+ selectivity increases moving from $Ru_{90}Pd_{10}$NPs to $Ru_{70}Pd_{30}$NPs to $Ru_{50}Pd_{50}$NPs. As we move to intermediate Pd-rich and very Pd-rich catalysts, the binding energy of NO_2^- continues to weaken;

on a $Ru_{25}Pd_{75}$ surface, the calculated binding energy of NO_2^- is only slightly weaker than the binding energy of H, so we would expect a slightly higher H surface coverage than NO_2^- surface coverage. Additionally, the thermodynamically favored pathway switches, and N–N formation becomes more favored than N–H formation. Consequently, the selectivity of $Ru_{30}Pd_{70}$NPs is a product of both effects, which is evidenced by the experimental results: 78.4% NH_4^+ and 21.6% N_2. As we continue to become more Pd-rich, the binding of NO_2^- becomes even weaker, but N–N formation also becomes much more favorable, and thermodynamics become more dominant resulting in a lower selectivity for NH_4^+ production.

5. Conclusion

We have shown that the end-product selectivity of aqueous NO_3^- reduction can be effectively and broadly controlled by varying the ratio of Ru:Pd in randomly alloyed Ru_xPd_{100-x}NP catalysts, supported on amorphous SiO_2. Although Ru and Pd are considered to be classically immiscible at room temperature across all compositions in bulk, metastable nanoalloys of Ru and Pd were confirmed using a variety of complementary spectroscopic techniques. Experimentally, we demonstrated that the selectivity of NO_3^- and NO reduction can be tuned by controlling the composition of RuPdNPs; specifically, a Ru-rich composition favors the formation of NH_4^+ and a Pd-rich composition favors N_2 formation. These results are supported by extensive DFT calculations of the thermodynamics of the competing pathways for NH_4^+ and N_2. However, the selectivity during NO_2^- reduction follows a slightly different trend where NH_4^+ selectivity peaks at ≈50% Ru. DFT calculations indicate this behavior is because the surface coverage of reactants plays a larger role than the thermodynamics of competing pathways during NO_2^- reduction compared to NO_3^- and NO reduction. Specifically, Ru-rich surfaces are susceptible to poisoning by NO_2^- coverage resulting in reduced activity and higher N_2 selectivity. Overall, in agreement with our original hypothesis, we prove that one must consider both the thermodynamics of competing pathways and the surface coverages of starting reactants when considering catalyst design for nitrate reduction. This provides an important lesson for those who pursue the future discovery of other new catalysts for industrially relevant reactions, where end-product selectivity is a critically important consideration.

Supporting Information

Supporting Information is available from the Wiley Online Library or from the author.

Acknowledgements

Conflict of Interest

The authors declare no conflict of interest.

Data Availability Statement

The data that support the findings of this study are available from the corresponding author upon reasonable request.

Keywords

density functional theory, microwave synthesis, nitrate reduction, noble metal catalysts, ruthenium-palladium alloys

[1] J. H. Clark, *Green Chem.* **1999**, *1*, 1.

[2] G. A. Somorjai, R. M. Rioux, *Catal. Today.* **2005**, *100*, 201.

[3] G. A. Somorjai, J. Y. Park, *Angew. Chem., Int. Ed.* **2008**, *47*, 9212.

[4] I. Lee, M. A. Albiter, Q. Zhang, J. Ge, Y. Yin, F. Zaera, *Phys. Chem. Chem. Phys.* **2011**, *13*, 2449.

[5] F. Zaera, *J. Phys. Chem. B.* **2002**, *106*, 4043.

[6] H. Li, S. Guo, K. Shin, M. S. Wong, G. Henkelman, *ACS Catal.* **2019**, *9*, 7957.

[7] H. Li, C. Yan, H. Guo, K. Shin, S. M. Humphrey, C. J. Werth, G. Henkelman, *ACS Catal.* **2020**, *10*, 7915.

[8] H. Guo, J. A. Trindell, H. Li, D. Fernandez, S. M. Humphrey, G. Henkelman, R. M. Crooks, *J. Mater. Chem. A.* **2020**, *8*, 8421.

[9] S. M. Davis, F. Zaera, G. A. Somorjai, *J. Am. Chem. Soc.* **1982**, *104*, 7453.

[10] P. Christopher, S. Linic, *AIChE Annu. Meet. Conf. Proc.* **2008**, 11264.

[11] J. B. Ernst, S. Muratsugu, F. Wang, M. Tada, F. Glorius, *J. Am. Chem. Soc.* **2016**, *138*, 10718.

[12] A. Fedorov, H. J. Liu, H. K. Lo, C. Copéret, *J. Am. Chem. Soc.* **2016**, *138*, 16502.

[13] L. J. Durndell, C. M. A. Parlett, N. S. Hondow, M. A. Isaacs, K. Wilson, A. F. Lee, *Sci. Rep.* **2015**, *5*, 9425.

[14] E. H. Boymans, P. T. Witte, D. Vogt, *Catal. Sci. Technol.* **2015**, *5*, 176.

[15] M. J. Taylor, L. J. Durndell, M. A. Isaacs, C. M. A. Parlett, K. Wilson, A. F. Lee, G. Kyriakou, *Appl. Catal. B.* **2016**, *180*, 580.

[16] B. Chen, F. Li, Z. Huang, G. Yuan, *Appl. Catal. B.* **2017**, *200*, 192.

[17] A. Liu, J. Ming, R. O. Ankumah, *Sci. Total Environ.* **2005**, *346*, 112.

[18] Y. Zhang, P. Shi, J. Song, Q. Li, *Appl. Sci.* **2018**, *9*, 18.

[19] R. Biddau, R. Cidu, S. Da Pelo, A. Carletti, G. Ghiglieri, D. Pittalis, *Sci. Total Environ.* **2019**, *647*, 1121.

[20] N. Kazakis, I. Matiatos, M. M. Ntona, M. Bannenberg, K. Kalaitzidou, E. Kaprara, M. Mitrakas, A. Ioannidou, G. Vargemezis, K. Voudouris, *Sci. Total Environ.* **2020**, *724*, 138211.

[21] B. T. Nolan, J. D. Stoner, *Environ. Sci. Technol.* **2000**, *34*, 1156.

[22] L. J. Puckett, *Environ. Sci. Technol.* **1995**, *29*, 408A.

[23] W. R. Raun, G. V. Johnson, *Agron. J.* **1999**, *91*, 357.

[24] L. Lassaletta, G. Billen, B. Grizzetti, J. Anglade, J. Garnier, *Environ. Res. Lett.* **2014**, *9*, 105011.

[25] K. R. Burow, B. T. Nolan, M. G. Rupert, N. M. Dubrovsky, *Environ. Sci. Technol.* **2010**, *44*, 4988.

[26] L. Pelletier, A. McFarlan, N. Maffei, *J. Power Sources.* **2005**, *145*, 262.

[27] C. Zamfirescu, I. Dincer, *J. Power Sources.* **2008**, *185*, 459.

[28] A. G. M. Da Silva, T. S. Rodrigues, S. J. Haigh, P. H. C. Camargo, *Chem. Commun.* **2017**, *53*, 7135.

[29] P. H. Pfromm, *J. Renew. Sustain. Energy.* **2017**, *9*, 034702.

[30] M. J. Palys, H. Wang, Q. Zhang, P. Daoutidis, *Curr. Opin. Chem. Eng.* **2021**, *31*, 100667.

[31] J. W. Erisman, M. A. Sutton, J. Galloway, Z. Klimont, W. Winiwarter, *Nat. Geosci.* **2008**, *1*, 636.

[32] S. L. Foster, S. I. P. Bakovic, R. D. Duda, S. Maheshwari, R. D. Milton, S. D. Minteer, M. J. Janik, J. N. Renner, L. F. Greenlee, *Nat. Catal.* **2018**, *1*, 490.

[33] L. Fewtrell, *Environ. Health Perspect.* **2004**, *112*, 1371.

[34] P. J. Weyer, J. R. Cerhan, B. C. Kross, G. R. Hallberg, J. Kantamneni, G. Breuer, M. P. Jones, W. Zheng, C. F. Lynch, *Epidemiology.* **2001**, *12*, 327.

[35] S. M. A. Adelana, *Water Encyclopedia.* **2005**, *4*, 30.

[36] A. R. Townsend, R. W. Howarth, F. A. Bazzaz, M. S. Booth, C. C. Cleveland, S. K. Collinge, A. P. Dobson, P. R. Epstein, E. A. Holland, D. R. Keeney, M. A. Mallin, C. A. Rogers, P. Wayne, A. H. Wolfe, *Front. Ecol. Environ.* **2003**, *1*, 240.

[37] C. J. Werth, C. Yan, J. P. Troutman, *ACS ES&T Eng.* **2021**, *1*, 6.

[38] M. Duca, M. T. M. Koper, *Energy Environ. Sci.* **2012**, *5*, 9726.

[39] H. Xu, Y. Ma, J. Chen, W. X. Zhang, J. Yang, *Chem. Soc. Rev.* **2022**, *51*, 2710.

[40] G. Yang, P. Zhou, J. Liang, H. Li, F. Wang, *Inorg. Chem. Front.* **2023**, *10*, 4610.

[41] S. Garcia-Segura, M. Lanzarini-Lopes, K. Hristovski, P. Westerhoff, *Appl. Catal. B.* **2018**, *236*, 546.

[42] Z. Wang, D. Richards, N. Singh, *Catal. Sci. Technol.* **2021**, *11*, 705.

[43] M. Duca, M. C. Figueiredo, V. Climent, P. Rodriguez, J. M. Feliu, M. T. M. Koper, *J. Am. Chem. Soc.* **2011**, *133*, 10928.

[44] S.-E. Bae, K. L. Stewart, A. A. Gewirth, *J. Am. Chem. Soc.* **2007**, *129*, 10171.

[45] T. Chen, H. Li, H. Ma, M. T. M. Koper, *Langmuir.* **2015**, *31*, 3277.

[46] Z. Wang, S. D. Young, B. R. Goldsmith, N. Singh, *J. Catal.* **2021**, *395*, 143.

[47] H. Begum, M. N. Islam, S. Ben Aoun, J. A. Safwan, S. S. Shah, M. A. Aziz, M. A. Hasnat, *Environ. Sci. Pollut. Res.* **2023**, *30*, 34904.

[48] M. N. Islam, M. Ahsan, K. Aoki, Y. Nagao, A. E. Alsafrani, H. M. Marwani, A. Almahri, M. M. Rahman, M. A. Hasnat, *J. Environ. Chem. Eng.* **2023**, *11*, 111149.

[49] X. Wu, M. Nazemi, S. Gupta, A. Chismar, K. Hong, H. Jacobs, W. Zhang, K. Rigby, T. Hedtke, Q. Wang, E. Stavitski, M. S. Wong, C. Muhich, J. H. Kim, *ACS Catal.* **2023**, *13*, 6804.

[50] S. Guo, H. Li, K. N. Heck, X. Luan, W. Guo, G. Henkelman, M. S. Wong, *Appl. Catal. B.* **2022**, *305*, 121048.

[51] S. Guo, K. Heck, S. Kasiraju, H. Qian, Z. Zhao, L. C. Grabow, J. T. Miller, M. S. Wong, *ACS Catal.* **2018**, *8*, 503.

[52] S. Hörold, K. D. Vorlop, T. Tacke, M. Sell, *Catal. Today.* **1993**, *17*, 21.

[53] S. D. Ebbesen, B. L. Mojet, L. Lefferts, *J. Catal.* **2008**, *256*, 15.

[54] H. Shin, S. Jung, S. Bae, W. Lee, H. Kim, *Environ. Sci. Technol.* **2014**, *48*, 12768.

[55] Y. Zhao, N. Koteswara Rao, L. Lefferts, *J. Catal.* **2016**, *337*, 102.

[56] K. Vorlop, T. Tacke, *Chemie Ing. Tech.* **1989**, *61*, 836.

[57] S. Hörold, T. Tacke, K. D. Vorlop, *Environ. Technol.* **1993**, *14*, 931.

[58] WHO, *Guidelines for Drinking-Water Quality, World Health Organization*, , **2017**.

[59] E. J. Bouwer, P. B. Crowe, *J. Am. Water Work. Assoc.* **1988**, *80*, 82.

**ADVANCED
SCIENCE NEWS**

www.advancedsciencenews.com

**NANO · MICRO
small**

www.small-journal.com

[60] R. G. Perkins, E. I. Slavin, T. M. C. Andrade, C. Blenkinsopp, P. Pearson, T. Froggatt, G. Godwin, J. Parslow, S. Hurley, R. Luckwell, D. J. Wain, *J. Environ. Manage.* **2019**, *244*, 276.

[61] L. Wei, D.-J. Liu, B. A. Rosales, J. W. Evans, J. Vela, *ACS Catal.* **2020**, *10*, 3618.

[62] X. Huo, D. J. Van Hoomissen, J. Liu, S. Vyas, T. J. Strathmann, *Appl. Catal. B.* **2017**, *211*, 188.

[63] K. Kusada, H. Kobayashi, R. Ikeda, Y. Kubota, M. Takata, S. Toh, T. Yamamoto, S. Matsumura, N. Sumi, K. Sato, K. Nagaoka, H. Kitagawa, *J. Am. Chem. Soc.* **2014**, *136*, 1864.

[64] N. Dahal, S. García, J. Zhou, S. M. Humphrey, *ACS Nano.* **2012**, *6*, 9433.

[65] S. Garcia, L. Zhang, G. W. Piburn, G. Henkelman, S. M. Humphrey, *ACS Nano.* **2014**, *8*, 11512.

[66] K. Kusada, H. Kobayashi, T. Yamamoto, S. Matsumura, N. Sumi, K. Sato, K. Nagaoka, Y. Kubota, H. Kitagawa, *J. Am. Chem. Soc.* **2013**, *135*, 5493.

[67] Y. Nanba, T. Ishimoto, M. Koyama, *J. Phys. Chem. C.* **2017**, *121*, 27445.

[68] H. Lin, H. Lin, J. X. Liu, H. Fan, W. X. Li, *J. Phys. Chem. C.* **2020**, *124*, 11005.

[69] Q. Zhang, K. Kusada, D. Wu, T. Yamamoto, T. Toriyama, S. Matsumura, S. Kawaguchi, Y. Kubota, H. Kitagawa, *Nat. Commun.* **2018**, *9*, 510.

[70] B. Huang, H. Kobayashi, T. Yamamoto, S. Matsumura, Y. Nishida, K. Sato, K. Nagaoka, M. Haneda, S. Kawaguchi, Y. Kubota, H. Kitagawa, *Chem. Sci.* **2020**, *11*, 11413.

[71] K. Sato, H. Tomonaga, T. Yamamoto, S. Matsumura, N. D. B. Zulkifli, T. Ishimoto, M. Koyama, K. Kusada, H. Kobayashi, H. Kitagawa, K. Nagaoka, *Sci. Rep.* **2016**, *6*, 28265.

[72] C. Song, A. Tayal, O. Seo, J. Kim, Y. Chen, S. Hiroi, L. S. R. Kumara, K. Kusada, H. Kobayashi, H. Kitagawa, O. Sakata, *Nanoscale Adv.* **2019**, *1*, 546.

[73] J. W. M. Frenken, P. Stoltze, *Phys. Rev. Lett.* **1999**, *82*, 3500.

[74] E. Ringe, R. P. Van Duyne, L. D. Marks, *Nano Lett.* **2011**, *11*, 3399.

[75] S. N. Tripathi, S. R. Bharadwaj, S. R. Dharwadkar, *J. Phase Equilib.* **1993**, *14*, 638.

[76] D. C. Harris, *Quantitative Chemical Analysis*, W. H. Freeman And Company, New York, NY, **2007**.

[77] H. Li, W. Chai, G. Henkelman, *J. Mater. Chem. A.* **2019**, *7*, 23868.

[78] C. D. Wagner, A. V. Naumkin, A. Kraut-Vass, J. W. Allison, C. J. Powell, J. R. Rumble, "NIST X-ray Photoelectron Spectroscopy Database, Version 4.1," DOI 10.18434/T4T88K can be found under https://srdata.nist.gov/xps, **2012**.

[79] D. J. Morgan, *Surf. Interface Anal.* **2015**, *47*, 1072.

[80] S. Seraj, P. Kunal, H. Li, G. Henkelman, S. M. Humphrey, C. J. Werth, *ACS Catal.* **2017**, *7*, 3268.

[81] P. Kunal, H. Li, B. L. Dewing, L. Zhang, K. Jarvis, G. Henkelman, S. M. Humphrey, *ACS Catal.* **2016**, *6*, 4882.

[82] J. P. Troutman, H. Li, A. M. Haddix, B. A. Kienzle, G. Henkelman, S. M. Humphrey, C. J. Werth, *ACS Catal.* **2020**, *10*, 7979.

[83] O. S. G. P. Soares, J. J. M. Órfão, J. Ruiz-Martínez, J. Silvestre-Albero, A. Sepúlveda-Escribano, M. F. R. Pereira, *Chem. Eng. J.* **2010**, *165*, 78.

[84] R. L. Vander Wal, T. M. Ticich, V. E. Curtis, *Carbon.* **2001**, *39*, 2277.

[85] M. E. Strayer, J. M. Binz, M. Tanase, S. M. Kamali Shahri, R. Sharma, R. M. Rioux, T. E. Mallouk, *J. Am. Chem. Soc.* **2014**, *136*, 5687.

[86] F. Epron, F. Gauthard, J. Barbier, *J. Catal.* **2002**, *206*, 363.

[87] N. Krawczyk, S. Karski, I. Witońska, *React. Kinet. Mech. Catal.* **2011**, *103*, 311.

[88] B. P. Chaplin, M. Reinhard, W. F. Schneider, C. Schüth, J. R. Shapley, T. J. Strathmann, C. J. Werth, *Environ. Sci. Technol.* **2012**, *46*, 3655.

[89] U. Prüsse, K. D. Vorlop, *J. Mol. Catal. A: Chem.* **2001**, *173*, 313.

[90] A. Pintar, M. Šetinc, J. Levec, *J. Catal.* **1998**, *174*, 72.

[91] F. A. Marchesini, S. Irusta, C. Querini, E. Miró, *Appl. Catal. A.* **2008**, *348*, 60.

[92] U. Prüsse, M. Hähnlein, J. Daum, K. D. Vorlop, *Catal. Today.* **2000**, *55*, 79.

[93] R. Zhang, D. Shuai, K. A. Guy, J. R. Shapley, T. J. Strathmann, C. J. Werth, *ChemCatChem.* **2013**, *5*, 313.

[94] R. S. Postma, R. Brunet Espinosa, L. Lefferts, *ChemCatChem.* **2018**, *10*, 3770.

[95] F. Engelke, R. Vincent, T. S. King, M. Pruski, *J. Chem. Phys.* **1994**, *101*, 7262.

[96] H. Zheng, H. Li, W. Song, Z. Zhao, G. Henkelman, *J. Phys. Chem. C.* **2021**, *125*, 12028.